Initial Electrodeposition Behavior of Chromium from Hydrate-Melt Based Trivalent Chromium Baths

Journal of The Electrochemical Society, 2023 **170** 062504

Initial Electrodeposition Behavior of Chromium from Hydrate-Melt Based Trivalent Chromium Baths

Haruki Katori,[1] Atsushi Kitada,[2] Kazuhiro Fukami,[1,*] and Kuniaki Murase[1,*,z]

[1]*Department of Materials Science and Engineering, Kyoto University, 36-1 Yoshida-hommachi, 606-8501, Kyoto, Japan*
[2]*Department of Chemical System Engineering, The University of Tokyo, 7-3-1 Hongo, 113-8656, Tokyo, Japan*

Trivalent chromium electrodeposition is expected to substitute the conventional hard chromium electroplating that requires harmful hexavalent chromium. Recently, we revealed that crystalline chromium, which is effective for hard chromium properties, can be electrodeposited from trivalent chromium baths using chloride-based hydrate-melts. Herein, we investigated the initial behavior of the trivalent chromium electrodeposition by in situ analyses using electrochemical quartz crystal microbalance (EQCM) and ex situ characterization of resulting electrodeposits. In the very initial stage of electrolysis, proton reduction proceeds preferentially, resulting in chromium hydroxide precipitation on the electrode due to the local pH increase. Chromium reduction was found to require a few seconds of induction time to start. The transient was interpreted by the Sand equation which also indicated proton depletion near the cathode. In the hydrate-melts, due to the depletion of free water, the high proton mobility due to Grotthuss mechanism is lost, resulting in the suppression of hydrogen evolution after the induction time. This explains why chromium electrodeposits are obtained at extremely high current efficiencies of 60%–80%. Additionally, the proton reduction of the initial electrolysis stage may lead to negative effects, for example, impairing adhesion of chromium electrodeposits.
 [DOI: 10.1149/1945-7111/acd9f0]

Manuscript submitted April 7, 2023; revised manuscript received May 14, 2023. Published June 16, 2023.

Supplementary material for this article is available online

Electroplated chromium is one of the most vital plated metals used for decorative and functional purposes due to its great corrosion resistance, hardness, and durability.[1] In the conventional industrial process, acidic sulfate baths containing hexavalent chromium, Cr (VI), is primarily used; however, due to its serious toxicity, there is a great demand for alternative processes using the less toxic trivalent chromium, Cr(III).[2] For decorative chromium plating, trivalent chromium baths using carbonate complexing agents are already in practical phase use, and are revealing details of chromium electrodeposition behaviors.[3–6] However, in such trivalent baths, the deposits are non-crystalline and contain carbides derived from complexing agents.[7,8] Thus, this process cannot be applied to hard chromium plating where crystalline chromium deposits with μm-order thicknesses are required for functional purposes.[1] Alternative processes for hard chromium plating using Cr(VI) baths are not yet established, thus the conventional hexavalent baths are still in practical use.

Recently our group reported a novel trivalent chromium plating using chloride-based hydrate-melt baths (i.e., highly concentrated aqueous electrolytes).[9,10] Several other studies have also suggested the availabilities of hydrate-melts for electrodeposition.[11,12] In the trivalent chromium baths using hydrate-melts, crystalline chromium deposits can be obtained despite the use of trivalent chromium, thus it is a promising substitute for hexavalent chromium plating. However, mechanical properties such as hardness, durability, and adhesion, are not completely identical to the conventional hard chromium plating. Further optimization of electrolysis condition, such as bath composition, and the selection of additives, including pH buffer, is required.

Regarding aqueous chromium electroplating, it is well known that the current efficiency of chromium is much lower compared to practical electroplating of other less-noble metals, such as zinc, tin, and nickel. In the case of hexavalent chromium plating using acidic sulfate baths, the current efficiency is 10%–25%,[1] and in the case of trivalent chromium plating using carbonate complexing agents, the current efficiency is even lower, around 10%.[5] There are several reasons for the low current efficiency of chromium electrodeposition: firstly, chromium has a negative electrode potential. According to the potential-pH diagram of Cr-H_2O system,[13] chromium electrodeposition appears to occur via the Cr^{2+} state, and the standard potential of Cr^{2+}/Cr^0 pair is very negative; –0.913 V vs standard hydrogen electrode (SHE). Therefore, thermodynamically favored hydrogen evolution proceeds during electrolysis, making chromium electrodeposition difficult. Secondly, trivalent chromium ion exchanges its ligands at a kinematically extremely slow speed.[14] As electrodeposition always involves desolvation, the current efficiency of chromium electrodeposition from trivalent chromium species is inevitably low.

In contrast, the current efficiency of our trivalent chromium electrodeposition using chloride-based hydrate-melts reaches 80%.[9] This value is anomalously high when compared to typical trivalent chromium electrodeposition. Suppression of hydrogen evolution due to free water depletion is considered a primary factor for this. In addition, trivalent chromium complexes involving chloride ions as ligands[15] are also an important factor. However, these factors correspond to bulk properties of the hydrate-melts, the local state at electrode-electrolyte interface also needs consideration to fully comprehend the process.

In general, pH near the cathode surface increases under hydrogen evolution, with the local environment differing to the bulk solution.[6,16] For example, in the case of hexavalent chromium electrodeposition using acidic sulfate baths, a "cathodic film" composed of trivalent chromium compounds is formed first, then chromium reduction proceeds through the film enabling the deposit to grow continuously.[17] Therefore, understanding the initial electrodeposition behavior influencing the environment of the electrode-electrolyte interface is important. In the initial stage of electrodeposition, the local pH increase caused by hydrogen evolution may contribute to a specific interface formation. This initial behavior is sometimes recorded, or encoded, in the precipitate obtained during the first stage of electrolysis. The precipitate formed at the interface between substrate and deposit may then influence practical and important issues such as adhesion of the deposited materials.

With the aim of inhibiting the hydroxide precipitation due to the local pH increase, boric acid is commonly used as a buffering agent, like Watts Ni electroplating using conventional acidic sulfate baths.[18] In the case of our hydrate-melts containing $CrCl_3$, the baths are highly acidic (see Table I) compared to Watts Ni plating bath,

*Electrochemical Society Member.
[z]E-mail: murase.kuniaki.2n@kyoto-u.ac.jp

Table I. Composition, pH, kinematic viscosity (ν) of H_2O–LiCl–$CrCl_3$ hydrate-melts at 40 °C.

n = H_2O/LiCl (molar ratio)	Composition (molar ratio) H_2O : LiCl : $CrCl_3$	pH	ν/mm^2 s^{-1}
3	55.5 : 18.5 : 1.0	<0	9.9
5	55.5 : 11.1 : 1.0	<0	3.9

but it is shown that boric acid allows the electrodeposition of metallic Cr without generating an electrochemically-inert chromium (III) hydrolytic oligomer.[9] However, it is still unclear whether the buffering effect is sufficient during the initial stage of electrolysis.

Several studies using the electrochemical quartz crystal microbalance (EQCM) technique, revealed the effect of boric acid during the electrodeposition of iron-group metals.[19,20] In the EQCM analyses, the mass change during electrodeposition is obtained using the Sauerbrey equation.[21] By comparing the mass change and amount of electricity during electrochemical measurements, non-faradic mass change (e.g., chemical precipitation of hydroxide due to hydrogen evolution) can be evaluated. Therefore, the EQCM is the best tool for analyzing and comparing the initial behavior of chromium electrodeposition, with and without boric acid.

In this study, in situ analyses using EQCM and ex situ analyses of the precipitate formed in the initial stage of electrolysis were performed to reveal chromium electrodeposition behavior specific to hydrate-melt baths. Several other electroanalytical techniques were also used in conjunction to evaluate the proton reduction behavior.

Experimental

Preparation of the hydrate-melt based chromium baths.—The H_2O–LiCl–$CrCl_3$ hydrate-melt with the H_2O/LiCl molar ratio (n) of 5 was primarily used. In evaluating proton reduction, another H_2O–LiCl–$CrCl_3$ melt with n = 3 was used for comparison. All reagents were used as purchased. Hydrate-melts were made by adding LiCl (98.0% purity, Nacalai Tesque) to deionized water. After that, $CrCl_3{\cdot}6H_2O$ (93.0% purity, FUJIFILM Wako Pure Chemical Corporation) was added to the H_2O–LiCl solutions to achieve the desired composition ($CrCl_3$ 1.0 mol kg^{-1}). To dissolve the chromium(III) salt and accelerate its ligand exchange, the solution was agitated with a magnetic stirrer at a speed of 500 rpm on a hot plate at 70 °C for at least one hour. pH and kinematic viscosity of the melts were measured using pH meter (HORIBA, LAQUAact D-71) with a conventional glass electrode, and Ubbelohde viscometer (SHIBATA, Ubbelohde SU). Composition, pH, and kinematic viscosity at 40 °C of the melts are summarized in Table I. In addition to the H_2O–LiCl–$CrCl_3$ melt, the H_2O–LiCl–$CrCl_3$–H_3BO_3 melt containing 30 g dm^{-3} of boric acid (99.5% purity, FUJIFILM Wako) was also prepared. The H_2O–$CaCl_2$–$CrCl_3$–H_3BO_3 melt was prepared by the same procedure using $CaCl_2$ (95% purity, FUJIFILM Wako), and used for EQCM measurements.

Electrochemical measurements.—Electrochemical measurements were carried out using a potentiostat (Bio-Logic Science Instruments, sp-300) with a three-electrodes cell. Gold (Au) layer vapor-deposited on a silicon wafer 15 mm × 15 mm with titanium underlayer was used as the working electrode for characterization of electrodeposits (see below), a glassy carbon sheet as the counter electrode, and Ag/AgCl in 3.33 mol dm^{-3} KCl aqueous solution with a salt bridge as the reference electrode. In the EQCM analyses, a quartz crystal (SEIKO EG&G, QA-A9M-AU) coated with Au 300 nm thick on both sides with a Ti underlayer was used as the working electrode. The quartz crystal electrode was mounted in a dip-type cell (SEIKO EG&G, QA-CL3) and immersed in the melts with only one side exposed. In this study, Au electrodes were used as the substrate, since Au is inert in the chromium bath and appropriate for analyzing the initial electrodeposition behavior. Hydrodynamic voltammetry was performed by a rotating electrode system (Hokuto Denko, DYNAMIC ELECTRODE HR-201) using a Pt disk (Hokuto Denko, HR2-D1-Pt5) as the working electrode. Pt is also inert and its high catalytic activity for H_2 evolution is beneficial to observe the proton limiting current for the RDE study. Before each electrochemical measurement, dissolved oxygen was removed by N_2 bubbling for 20 min, and the melt temperature was maintained at 40 °C using a thermostatic bath.

Characterization of electrodeposits.—For characterization of electrodeposits, electrolysis was performed using the above-mentioned Au layer on Si. Transmission electron microscopy (TEM) analysis using a JEOL JEM-2100F and energy dispersive X-ray spectrometry (EDS) were carried out for cross-sectional observation. Samples were prepared for the observation by focus ion beam (FIB) using a FEI Quanta 200 3DS. The composition and chemical states of deposits and precipitates were characterized by X-ray photoelectron spectroscopy (XPS) using a JEOL JPS-9010TRX.

Results and Discussion

EQCM study.—In EQCM analyses, frequency and resonance resistance were recorded simultaneously with electrochemical measurements. The change in frequency Δf_m corresponds to a mass change Δm in accordance with the Sauerbrey equation:

$$\Delta f_m = -\frac{2f_0^2}{A\sqrt{\mu_q \rho_q}}\Delta m \qquad [1]$$

where f_0 is the resonance frequency (9.00 MHz), A is the electrode area (0.196 cm^2), ρ and μ are the density (2.65 g cm^{-3}) and elastic coefficient (2.95 × 10^{11} g cm^{-1} s^{-2}) of the quartz, respectively. Therefore, the mass sensitivity of the electrode used in the experiment is –1.07 ng/Hz. The resonance resistance reflects the density and the viscosity of electrolyte in the vicinity of electrode, and is represented by the equation:

$$R = \frac{A\sqrt{2\pi f_0 \mu_L \rho_L}}{k^2} \qquad [2]$$

where k is the electromechanical coupling factor, μ_L and ρ_L are the density and viscosity of the electrolyte, respectively. In the situation where the properties of electrolytes near the electrode change, the amount of change in resonance resistance ΔR contributes to the frequency as $\Delta f_{\mu\rho}$ given by a coefficient B (6.2 Hz Ω^{-1}) specific to the electrode:

$$\Delta f_{\mu\rho} = -B\Delta R \qquad [3]$$

The data of frequency change Δf is composed of Δf_m and $\Delta f_{\mu\rho}$ (Eq. 4), therefore, Δf_m was obtained from Δf by subtracting the contribution of $\Delta f_{\mu\rho}$.

$$\Delta f = \Delta f_m + \Delta f_{\mu\rho} \qquad [4]$$

This procedure is proposed in several papers investigating minute mass change during electrodeposition.[22,23] Chromium electrodeposition generally accompanies hydrogen evolution, i.e., a gas evolution at the electrode surface, and resonance resistance is expected to decrease significantly. Therefore, it is necessary to subtract the contribution of resonance resistance in order to accurately evaluate

the mass change through the measurements. As a preliminary experiment for this study, it was confirmed that the mass change can be evaluated even under gas evolution, by using a dilute HCl electrolyte without $CrCl_3$, and monitoring hydrogen gas evolution (see Fig. S1). The change in frequency Δf_m obtained by Eq. 4 indicated zero although resonance resistance decreased continuously under hydrogen gas evolution. The change in resonant resistance corresponds to a local decrease in the apparent density and viscosity of electrolyte owing to H_2 bubbles attached to the electrode. In addition to the effects of electrolyte properties, the resonance resistance also reflects the effects of surface roughness and internal stress of the deposits formed during electrolysis. In this study, these effects are also considered.

In the cathodic galvanostatic electrolysis, the change in current efficiency over time was determined assuming a three-electron reduction of trivalent chromium and Faraday's law:

$$\eta = \frac{\Delta m}{M}\frac{3F}{Q} \times 100 \qquad [5]$$

where η is current efficiency, Q is the charge passed during electrolysis, M is the molecular weight (in this case 52.0 g mol^{-1}), and F is the Faraday constant.

EQCM analyses of cathodic sweep voltammetry.—Cathodic voltammograms obtained with the QCM electrode (Au) at 10 mV s^{-1} in H_2O–LiCl–$CrCl_3$ melts ($n = 5$) with or without boric acid are shown in Fig. 1a. The concomitant change in frequency Δf_m and resonance resistance ΔR are also shown in Figs. 1b–1c.

As in the previous paper,[9] a suppressed proton reduction wave at a potential range of –0.3 to –1.0 V and subsequent onset of the chromium reduction at –1.1 V were observed. Corresponding to a rise of the proton reduction at –0.3 V, the resonance resistance R decreased rapidly. This is due to a decrease in the apparent density and viscosity of electrolytes near the electrode owing to H_2 bubbles attachment. In fact, immediately after the potential sweep, grown bubbles were visually observed on the electrode. In the potential range of –0.3 to –1.0 V, the negative frequency change Δf_m revealed that the electrode mass slightly increased in response to the progress of proton reduction. As metallic Cr cannot electrodeposit in this potential range, this change in Δf_m is attributed to the non-faradic precipitation of chromium hydroxide accompanying the local increase in pH. Importantly, the same results were obtained in the bath with and without boric acid, suggesting that the addition of boric acid does not completely suppress the hydroxide precipitation under hydrogen evolution. Upon potentiostatic electrolysis at –1.0 V using the chromium bath containing boric acid, a translucent precipitate was obtained. XPS analysis confirmed that the precipitate was composed of chromium hydroxide (see Fig. S2 and Table SI).[24] After that, a rapid increase in electrode mass was observed at potentials more negative than –1.1 V, corresponding to a rise of the chromium reduction current. The resonance resistance R began to increase at around –1.0 V, and is due to the suppression of proton reduction and also detachment of H_2 bubbles from the electrode. In addition, contributions of the deposit properties such as surface roughness and internal stress are also conceivable.

EQCM analyses of galvanostatic electrolysis.—EQCM analyses of galvanostatic electrolysis on the QCM electrode (Au) at a cathodic current density of 50 mA cm^{-2} in H_2O–LiCl–$CrCl_3$ melts ($n = 5$) with or without boric acid were conducted. The change in electrode potential E over time (i.e., E–t profile) and concomitant changes in frequency Δf_m and resonance resistance ΔR, and current efficiency η are shown in Figs. 2a–2d. The inset of Fig. 2b shows the change in frequency during the initial stage of electrolysis.

In the first stage of electrolysis, the electrode mass hardly changed for a few seconds; instead, the resonance resistance R decreased rapidly. The electrode potential did not reach the potential at which chromium reduction proceeds, suggesting that only proton

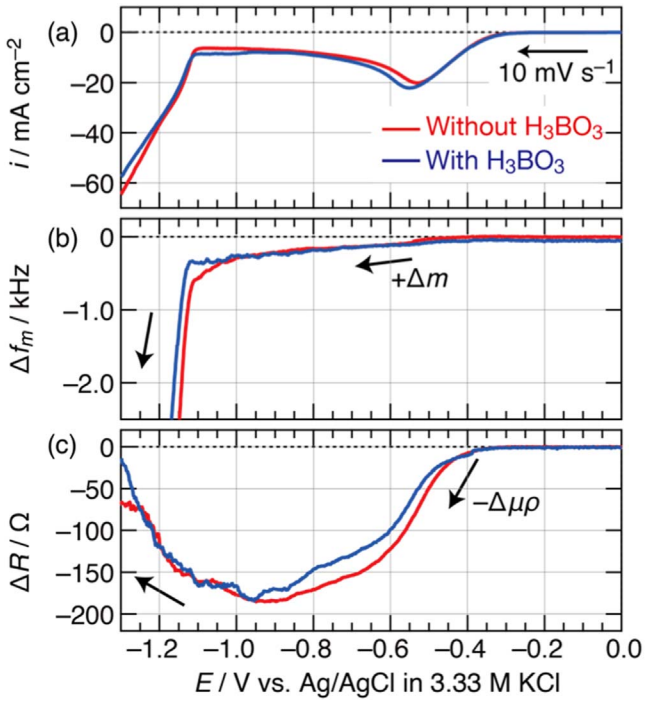

Figure 1. EQCM results for cathodic voltammetry of the H_2O–LiCl–$CrCl_3$ hydrate-melts ($n = 5$) with or without H_3BO_3 at 40 °C measured at a scan rate of 10 mV s^{-1}; (a) voltammogram, (b) change in frequency, and (c) change in resonant resistance.

reduction occurred during this short period. The current efficiency in the period was almost zero. However, small mass changes were observed during this period, indicating the precipitation of chromium hydroxide on the substrate surface due to local pH increase (see the inset of Fig. 2b). Then, the electrode potential shifted rapidly, corresponding to chromium reduction, and the electrode mass began to increase. During chromium reduction, the resonant resistance ceased to decrease since the detachment of H_2 bubbles occurred simultaneously with hydrogen gas evolution. In addition, it was conceivable that contribution of the deposit such as surface roughness and internal stress also increased the resonance resistance. The current efficiency also began to increase, exceeding 50% after 20 s of electrolysis. Thereafter, the current efficiency remained stable, suggesting steady growth of the chromium layer. If the amount of co-deposited hydroxide (i.e., excessive non-faradic mass change) differs between the baths with and without boric acid, the current efficiency may reflect its contribution. However, appreciable differences were not observed from multiple experiments.

The same experiments as Figs. 1 and 2 for the H_2O–LiCl–$CrCl_3$ melt were performed for the H_2O–$CaCl_2$–$CrCl_3$ melt containing boric acid. The trend of results was the same for the $CaCl_2$–based melts: In linear sweep voltammetry, it was observed that electrode mass changed slightly with hydrogen evolution, even in the electrolyte containing boric acid (Fig. S3), and that there is an induction time leading to chromium reduction for cathodic galvanostatic electrolysis by EQCM analyses (Fig. S4).

Cross-sectional observation.—Cross-sectional STEM images of chromium deposits obtained by galvanostatic electrolysis at a cathodic current density of 50 mA cm^{-2} for 1 min on Au electrode using the H_2O–LiCl–$CrCl_3$ melts ($n = 5$) with or without boric acid are shown in Fig. 3.

In the deposit from the melt without boric acid, some amorphous domains were observed, while most of the deposit consisted of crystalline chromium with a BCC-structure. This was revealed by nano beam diffraction (NBD), and the dark contrast area corresponds to the crystalline domain (Fig. S5). The bright contrast area

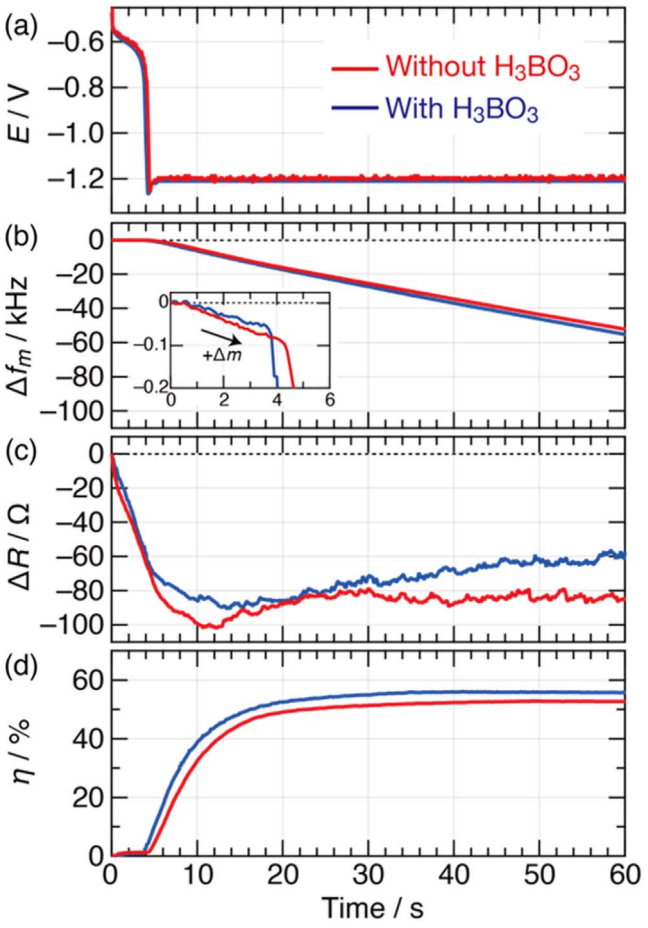

Figure 2. EQCM results for cathodic galvanostatic electrolysis at 50 mA cm^{-2} using the H_2O–LiCl–$CrCl_3$ hydrate-melts (n = 5) with or without H_3BO_3 at 40 °C; change in (a) electrode potential, (b) frequency, (c) resonant resistance, and (d) current efficiency. The inset shows change in frequency during the initial stage of electrolysis, indicating small mass changes under hydrogen evolution.

located around the center of the image shown in Fig. 3a corresponds to the amorphous domain, and in this area, oxygen (O) was detected at much higher concentration compared with the crystalline area by EDS analyses, suggesting that the amorphous structure is primarily composed of chromium hydroxide (Fig. S6 and Table SII). The image of the deposit from the melt containing H_3BO_3 (Fig. 3b) shows that boric acid suppresses the precipitation of chromium hydroxide. The result that bulk co-deposition of hydroxide with metallic Cr is significantly suppressed by adding boric acid is consistent with our previous work.[9] On the other hand, for deposits obtained from both melts with and without H_3BO_3, amorphous structures were observed in the immediate vicinity of the Au substrate (Fig. 4). By EDS analyses, it was found that these structures contain much more O compared with the crystalline area (Fig. S6 and Table SII). They correspond to chromium hydroxide formed because of hydrogen evolution in the initial few seconds of electrolysis.

Considering the results of cross-sectional observation and EQCM analyses, it is revealed that boric acid suppresses the precipitation of chromium hydroxide during chromium reduction, but does not affect the polarization behavior and hydroxide precipitation in the initial stage of electrolysis. It is considered that the precipitation on the Au substrate is due to the high proton reduction rate before reaching its diffusion limit, where boric acid does not work. On the other hand, the suppression of hydroxide co-deposition with the bulk Cr layer implies the possibility that boric acid suppresses the local pH increase during chromium reduction. In general, it is interpreted that boric acid suppresses the precipitation of hydroxide primarily by its buffering effect.[18,25] However, several reports have mentioned other characteristic effects of boric acid. Rigsby et al. demonstrated the role of boric acid exerted by adsorption on the electrode surface apart from its pH buffering.[26] On the other hand, several studies suggested the complexation between Ni(II) and boric acid in typical aqueous solutions.[27,28] As seen above, the function of boric acid depends on its context, for example, electrolyte composition, pH, and electrode potential. The environment of hydrate-melts where free water is extremely depleted may also affect the behavior of boric acid. Thus, it is difficult to apply the previous observations to the hydrate-melt based chromium electrodeposition. A further study with more focus on the function of boric acid in hydrate-melts is expected.

Evaluation of proton reduction.—Figure 5 shows the cathodic linear sweep voltammograms using rotating disc electrode (RDE) of Pt (diameter 5 mm) at 5 mV s^{-1} in the H_2O–LiCl–$CrCl_3$ melt. The voltammograms were measured at five different rotating rates between 250 and 2000 rpm. The inset shows the relationship between the rotating rate and the limiting current density; here, as is well known in RDE electrochemistry, the limiting current density $|i_L|$ varies linearly with the root of the angular velocities $\omega^{1/2}$ in

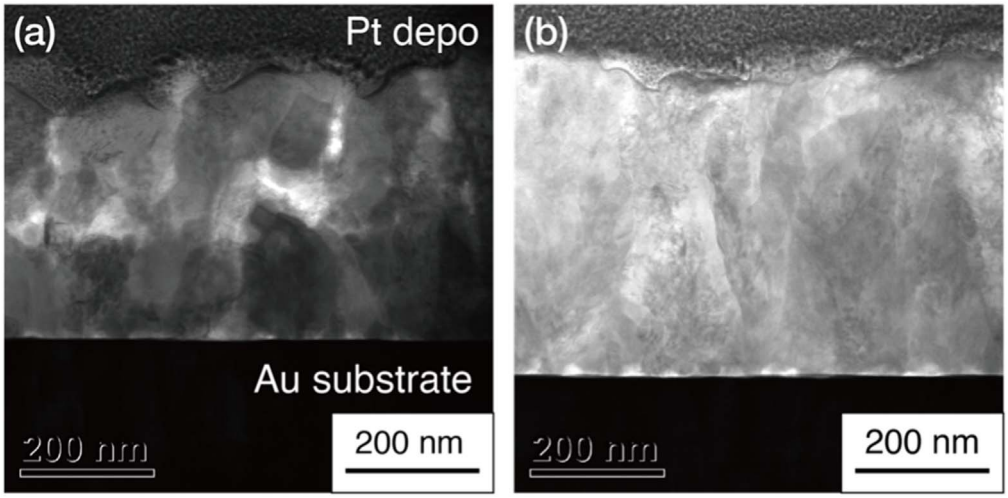

Figure 3. STEM images of the deposits prepared by cathodic galvanostatic electrolysis at 50 mA cm^{-2} using the H_2O–LiCl–$CrCl_3$ hydrate-melts (n = 5) (a) without or (b) with H_3BO_3 at 40 °C.

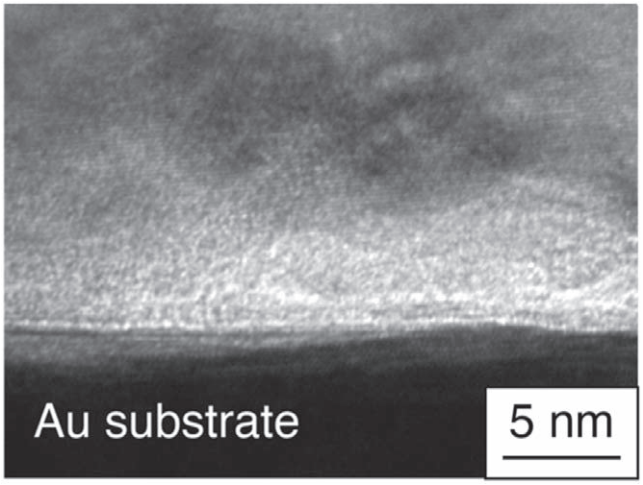

Figure 4. HR-TEM image of the deposit prepared by cathodic galvanostatic electrolysis at 50 mA cm^{-2} using the H_2O–LiCl–$CrCl_3$ hydrate-melt ($n = 5$) with H_3BO_3 at 40 °C.

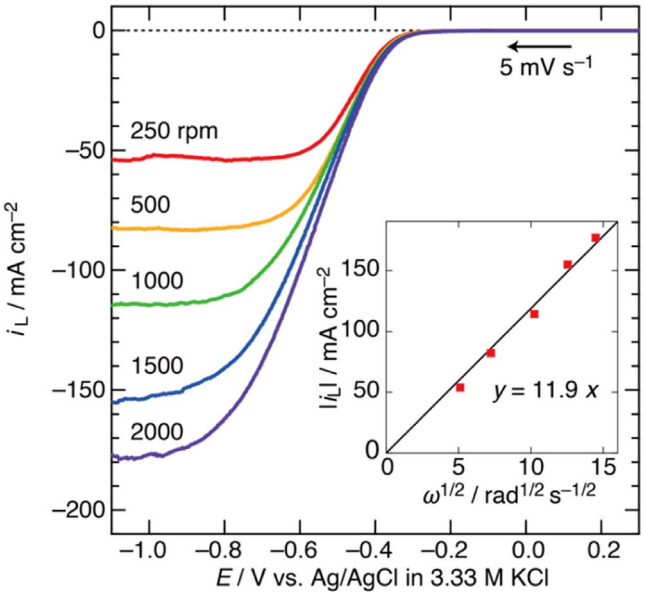

Figure 5. A set of linear sweep voltammograms for the H_2O–LiCl–$CrCl_3$ hydrate-melts ($n = 5$) at 40 °C measured at a scan rate of 5 mV s^{-1} using a Pt RDE with five different rotating rates. The inset shows the Levich plot.

accordance with the Levich equation:

$$i_L = 0.62zFcD^{2/3}\nu^{-1/6}\omega^{1/2} \quad [6]$$

where z represents the number of electrons involved in the reduction (in this case $z = 2$), F is the Faraday constant, c is the bulk concentration of reactant (H^+ in this case), D is the diffusion coefficient, and ν is the kinematic viscosity.[29] The Levich plot shows good linearity of $|i_L|$ to $\omega^{1/2}$, indicating that proton reduction was suppressed by diffusion limitation in hydrate-melt baths. In very acidic aqueous solutions, for example pH < 0, proton reduction rarely reaches the diffusion limit. This is even more so since proton generally has large mobility due to the Grotthuss mechanism.[30] The small but distinct limiting current of about 10 mA cm^{-2}, despite the high acidity of the melt, means that the actual concentration of proton c is low and the Grotthuss mechanism is lost. The proton concentration is not large enough to be comparable to the proton activity as indicated by the glass electrode pH < 0, implying that the proton activity coefficient in hydrate-melts is large.

In order to evaluate the bulk concentration c and diffusion coefficient D of proton, the initial stage of cathodic galvanostatic electrolysis for the H_2O–LiCl–$CrCl_3$ melt was analyzed using the Au electrode. Figure 6 shows the potential vs time profile in the initial stage of the electrolysis at three different cathodic current densities between 40 and 60 mA cm^{-2}. In the case of galvanostatic electrolysis at a current density beyond the limiting current density for a given reaction, a potential transition is observed from the reaction to another less noble reaction. The relationship between the induction time τ and current density i_c is given by the Sand equation:[31]

$$|i_c|\ \sqrt{\tau} = \frac{1}{2}zFc\sqrt{\pi D} \quad [7]$$

In Fig. 6, a clear transition from the proton reduction, a noble reaction, to the chromium reduction, a less noble reaction, was observed at τ of 2.2 s (60 mA cm^{-2}) to 5.0 s (40 mA cm^{-2}). The relationship between $\tau^{-1/2}$ and $|i_c|$ was in good agreement with the Sand equation, indicating that the induction to the chromium reduction takes place upon the proton reduction reaching the diffusion limit. From the Levich and Sand equations, the proton concentration $c = 0.38$ mol L^{-1} and diffusion coefficient $D = 1.9 \times 10^{-6}$ cm^2 s^{-1} were obtained. The diffusion coefficient is about one fiftieth smaller compared to that in dilute aqueous solution;[32] $D = 9.3 \times 10^{-5}$ cm^2 s^{-1}, and is consistent with the previously reported experimental value.[33] The diffusion coefficient of Cu^{2+} cation in the LiCl hydrate-melt bath 5.47×10^{-6} cm^2 s^{-1} (in 8 mol L^{-1} LiCl) has the same order of magnitude.[33] Therefore, the Grotthuss mechanism, that is fast proton hopping through hydrogen bond network of water molecules, is suppressed in the melt and the proton diffusion is slowed down remarkably due to the depletion of free water.By the same procedure (Figs. S7–S8), using the Levich and Sand equations, the proton concentration and diffusion coefficient of the $n = 3$ melt were obtained: $c = 0.54$ mol L^{-1}, and $D = 2.8 \times 10^{-7}$ cm^2 s^{-1}, suggesting that the proton reduction is further suppressed with the increase of LiCl concentration. Figure 7 shows the change in current efficiency during galvanostatic electrolysis at a cathodic current density of 50 mA cm^{-2} in the H_2O–LiCl–$CrCl_3$ melts of $n = 3$ and $n = 5$. In the $n = 3$ melt, the time required for proton depletion was shorter, and the chromium deposition proceeded at a higher current efficiency, close to 80%. This is due to further suppression of proton diffusion through the decrease in free water and increase in electrolyte viscosity. All the above indicates that, in the chromium electrodeposition using hydrate-melts, the increase in chloride concentration has advantages not only in increasing the current efficiency of chromium deposition, but also in suppressing hydrogen generation in the initial stage of electrolysis.

Conclusions

Trivalent chromium electrodeposition using hydrate-melt baths is noted as novel plating process for hard chromium plating process. In the present study, it is revealed that proton reduction preferentially occurs during the very initial stage of electrolysis and chromium hydroxide precipitates near the substrate, by in situ analyses using EQCM and characterization of deposits. Boric acid suppresses the bulk co-deposition of hydroxide with metallic Cr, however, its function is not sufficient for suppressing the precipitation of hydroxide during the initial stage of electrolysis. Therefore, it is important to note that this may affect properties including adhesion of the deposits in practice. In the initial stage of galvanostatic electrolysis, a few seconds of induction time leading to chromium reduction is required. The transient was interpreted by the Sand equation, indicating the proton depletion near the cathode. The diffusion coefficient of proton in hydrate-melts evaluated by the Sand and Levich equations was much smaller compared to the one in typical aqueous solutions. In hydrate-melts, due to the depletion of free water, the fast proton diffusion owing to Grotthuss mechanism is inhibited, resulting in extremely high current efficiency of trivalent chromium electrodeposition.

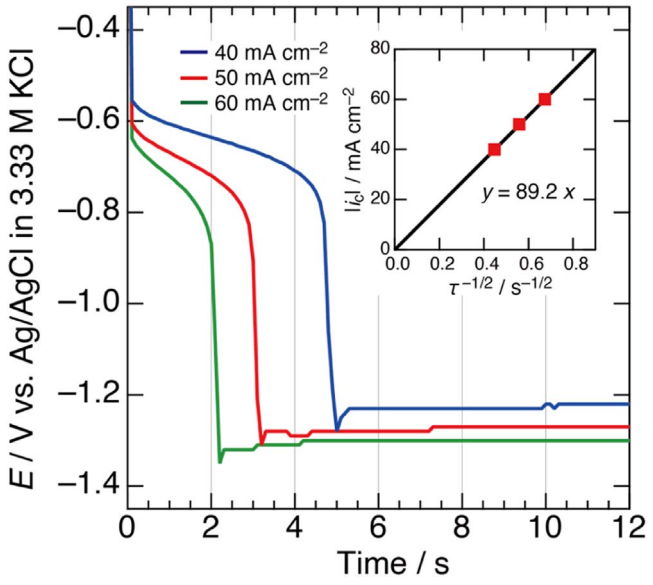

Figure 6. Change in electrode potential over time (i.e., *E*-*t* profile) during the initial stage of cathodic galvanostatic electrolysis at 40–60 mA cm^{-2} using the H_2O–LiCl–$CrCl_3$ hydrate-melt ($n = 5$) at 40 °C. The inset shows the $|i_c|$ vs $\tau^{-1/2}$ plot.

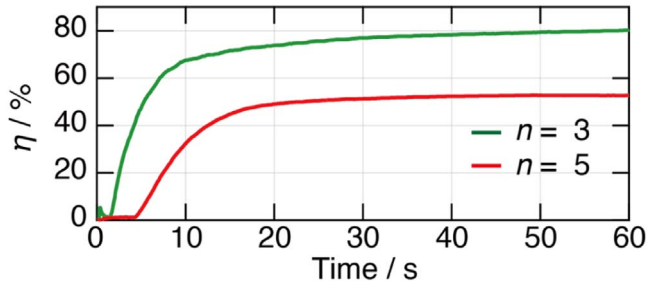

Figure 7. Change in current efficiency during cathodic galvanostatic electrolysis at 50 mA cm^{-2} using the H_2O–LiCl–$CrCl_3$ hydrate-melts ($n = 3$, 5) at 40 °C.

Acknowledgments

The authors acknowledge Mr. Yutaka Sonobayashi (Kyoto University) for supporting the XPS measurements, and Mr. Kenji Kazumi (Kyoto University) for supporting the TEM measurements. This work was supported financially by Grants-in-Aid for Scientific Research (S) (No. 20H05663: K. M.) from the Japan Society for the Promotion of Science, Nakanishi Scholarship Foundation, and JST, the establishment of university fellowships towards the creation of science technology innovation (Grant Number JPMJFS2123).

ORCID

Haruki Katori https://orcid.org/0009-0002-7761-5006
Atsushi Kitada https://orcid.org/0000-0002-4387-8687
Kazuhiro Fukami https://orcid.org/0000-0001-9120-5578
Kuniaki Murase https://orcid.org/0000-0002-7564-9416

References

1. M. Schlesinger and M. Paunović, *Modern Electroplating* (Wiley, New York) p. 205 (2011).
2. B. O. Okonkwo, C. Jeong, and C. Jang, *Coatings*, **12**, 1555 (2022).
3. A. Baral and R. Engelken, *J. Electrochem. Soc.*, **152**, C504 (2005).
4. D. Del Pianta, J. Frayret, C. Gleyzes, C. Cugnet, J. C. Dupin, and I. Le Hecho, *Electrochim. Acta*, **284**, 234 (2018).
5. Y. B. Song and D. T. Chin, *Electrochim. Acta*, **48**, 349 (2002).
6. M. Leimbach, C. Tschaar, U. Schmidt, and A. Bund, *Electrochim. Acta*, **270**, 104 (2018).
7. A. M. Liang, L. W. Ni, Q. Liu, and J. Y. Zhang, *Surf. Coat. Technol.*, **218**, 23 (2013).
8. F. I. Danilov, V. S. Protsenko, V. O. Gordiienko, S. C. Kwon, J. Y. Lee, and M. Kim, *Appl. Surf. Sci.*, **257**, 8048 (2011).
9. K. Adachi, A. Kitada, K. Fukami, and K. Murase, *Electrochim. Acta*, **338**, 135873 (2020).
10. Y. Yoshikane, H. Seto, J. Katayama, T. Nagao, R. Oosawa, A. Kitada, and K. Murase, *J. Surf. Finish. Soc. Jpn.*, **71**, 815 (2020).
11. K. Matsumoto, J. Zhang, N. Yoneda, K. Numata, K. Okuno, and R. Hagiwara, *J. Phys. Chem. C*, **126**, 14346 (2022).
12. K. Adachi, A. Kitada, K. Fukami, and K. Murase, *J. Electrochem. Soc.*, **166**, D409 (2019).
13. M. Pourbaix, *Atlas of electrochemical equilibria in aqueous solutions* (National Association of Corrosion Engineers, Houston, Texas) 2nd ed. p. 256 (1974).
14. R. A. Plane and H. Taube, *J. Phys. Chem.*, **56**, 33 (1952).
15. M. J. Bjerrum and J. Bjerrum, *Acta Chem. Scand.*, **44**, 358 (1990).
16. M. Motoyama, Y. Fukunaka, T. Sakka, and Y. H. Ogata, *J. Electrochem. Soc.*, **153**, C502 (2006).
17. N. V. Mandich, *Plat. Surf. Finish.*, **84**, 97 (1997).
18. M. Schlesinger and M. Paunović, *Modern Electroplating* (Wiley, New York) p. 103 (2011).
19. K. D. Song, K. B. Kim, S. H. Han, and H. K. Lee, *Electrochem. Commun.*, **5**, 460 (2003).
20. J. S. Santos, R. Matos, F. Trivinho-Strixino, and E. C. Pereira, *Electrochim. Acta*, **53**, 644 (2007).
21. G. Sauerbrey, *Z. Phys.*, **155**, 206 (1959).
22. N. Serizawa, Y. Katayama, and T. Miura, *J. Electrochem. Soc.*, **156**, D503 (2009).
23. K. Fukami et al., *Electrochem. Commun.*, **136**, 107238 (2022).
24. M. C. Biesinger, C. Brown, J. R. Mycroft, R. D. Davidson, and N. S. McIntyre, *Surf. Interface Anal.*, **36**, 1550 (2004).
25. J. Ji, W. C. Cooper, D. B. Dreisinger, and E. Peters, *J. Appl. Electrochem.*, **25**, 642 (1995).
26. M. A. Rigsby, T. A. Spurlin, and J. D. Reid, *J. Electrochem. Soc.*, **167**, 112507 (2020).
27. B. V. Tilak, A. S. Gendron, and M. A. Mosoiu, *J. Appl. Electrochem.*, **7**, 495 (1977).
28. A. Graff, E. Barrez, P. Baranek, M. Bachet, and P. Bénézeth, *J. Solut. Chem*, **46**, 25 (2017).
29. A. J. Bard and L. R. Faulkner, *Electrochemical Methods* (Wiley, New York) 2nd ed. p. 337 (2001).
30. N. Agmon, *Chem. Phys. Lett.*, **244**, 456 (1995).
31. A. J. Bard and L. R. Faulkner, *Electrochemical Methods* (Wiley, New York) 2nd ed. p. 308 (2001).
32. W. M. Haynes, *CRC Handbook of Chemistry and Physics* (CRC press) 96th ed. (2015).
33. S. De, J. White, T. Brusuelas, C. Patton, A. Koh, and Q. Huang, *Electrochim. Acta*, **338**, 135852 (2020).